PHYSICAL REVIEW B **94**, 174302 (2016)

Transport properties in dilute UN(X) solid solutions (X = Xe, Kr)

Antoine Claisse,[1,*] Thomas Schuler,[2] Denise Adorno Lopes,[1] and Pär Olsson[1]
[1]*Reactor Physics, KTH-Royal Institute of Technology, Stockholm, Sweden*
[2]*Department of Materials Science and Engineering, University of Illinois, Urbana-Champaign, Illinois 61801, USA*

(Received 18 August 2016; published 4 November 2016)

Uranium nitride (UN) is a candidate fuel for current GEN III fission reactors, for which it is investigated as an accident-tolerant fuel, as well as for future GEN IV reactors. In this study, we investigate the kinetic properties of gas fission products (Xe and Kr) in UN. Binding and migration energies are obtained using density functional theory, with an added Hubbard correlation to model f electrons, and the occupation matrix control scheme to avoid metastable states. These energies are then used as input for the self-consistent mean field method which enables to determine transport coefficients for vacancy-mediated diffusion of Xe and Kr on the U sublattice. The magnetic ordering of the UN structure is explicitly taken into account, for both energetic and transport properties. Solute diffusivities are compared with experimental measurements and the effect of various parameters on the theoretical model is carefully investigated. We find that kinetic correlations are very strong in this system, and that despite atomic migration anisotropy, macroscopic solute diffusivities show limited anisotropy. Our model indicates that the discrepancy between experimental measurements probably results from different irradiation conditions, and hence different defect concentrations.

DOI: 10.1103/PhysRevB.94.174302

I. INTRODUCTION

Uranium nitride (UN) has been proposed as an accident-tolerant fuel for current GEN II and III nuclear reactors, as well as for future GEN IV and space reactors. This fuel presents various interesting properties such as high fissile density, excellent thermal conductivity, and good tolerance for minor actinide inclusion. However, experimental data on nitride fuels is scarce since it suffers from several drawbacks: it should optimally be enriched in ^{15}N, it was believed not to be compatible with water until a recent study in steam [1], and the focus has historically been on oxide fuels. Modeling has an important role to play in the characterization, choice of experiments, and licensing process, especially because experimental fuel testing is expensive and burdensome (need for hot cells). Nevertheless, various past experiments have been dedicated to the measure of Xe and Kr diffusion in UN, and the data have been reviewed by Deforest [2]. The results show discrepancies of several orders of magnitude at usual operating temperatures (under 1000 K), which might be attributed to different sample purity, measurement methods, irradiation conditions, and samples being either monocrystals or polycrystals. Among these values, modeling can bring some insight in migration mechanisms and provides estimate values for diffusion coefficients in various conditions.

Energetic properties (formation, binding, and migration energies) in $5f$ materials are challenging to compute properly due to the strong correlation between electrons that is not taken into account correctly in conventional density functional theory (DFT). Methods such as the dynamical mean field theory are supposed to provide a much better description of strongly correlated materials, but are still too computationally demanding to model hundreds of atoms in a systematic way, and so far, only bulk studies have been done [3,4]. A more suitable correction to DFT has been proposed, by adding an *ad hoc* correlation term, in a method known as DFT + U [5]. A drawback of this method is that it has been shown to introduce local minima known as metastable states [6], that have to be dealt with. These states are purely numerical and carry little physical meaning. Hence, converging to one of them should be avoided. This can be done using several schemes: ramping [6,7], quasiannealing [8], controlled symmetry reduction [9], and occupation matrix control (OMC) [10], for instance. Most of them have been used to model UN systems [11–13]. In an extensive study of the ground state and metastable states in bulk UN, the OMC method has been shown to be adequate [12]. In this study, the ground state at low temperature has been found to be antiferromagnetic for an introduced correlation greater than about 1.8 eV and the structure has been computed to be an orthorhombic rocksalt. The OMC and geometry reported in Ref. [12] have been used in this work.

Point defects in UN have been investigated with various methods, using either generalized gradient approximation (GGA) or GGA + U or interatomic potentials to compute the formation energies of various vacancy, antisite, Frenkel and Schottky defect configurations [14–16]. They were found to be different depending on the studies and methods used, but in the most comprehensive of them [15], the formation energy of a U vacancy, an N vacancy, and a Schottky defect were found to be, respectively, 6.89, 7.81, and 13.81 eV, using GGA + U ($U_{\text{eff}} = 1.85$ eV) and the isolated atoms as reference states. The incorporation energy of Xe in various defects has been investigated in previous studies [12,17], showing that it is most stable in a Schottky defect if these defects already exist. Taking into account the formation energies reported above and the incorporation energies of these studies, the lowest solution energy was found to be for Xe in a uranium vacancy. In a recent study, vacancy-mediated diffusion of Xe in UN was studied, and a few migration paths were considered [18] using the quasiannealing approach to deal with metastable states introduced in the DFT + U scheme.

---

[*] Corresponding author: claisse@kth.se

The diffusion of xenon in other types of nuclear fuels has also been studied. The work on silicide [19–22] or carbide [23] is only starting, but the work on oxide fuels has already received many contributions. It is outside the scope here to mention all of them, but Xe has been studied in UO_2 [24], other actinide oxide fuels [25], and its diffusion following complex paths has also been investigated [26], as well as the effect of nonstoichiometry and irradiation conditions on its diffusion properties [27]. However, krypton has never been considered in such works either for UN, except when swelling was the sole phenomenon being investigated [17]. Even in some fuel performance codes, Xe and Kr are assumed to have the same coefficient [28], an assumption that merits verification.

Historically, the modeling of diffusion in actinide compounds considered simple Arrhenius laws or Le Claire's model [20,23]. However, the influence of the magnetic ordering has never been studied and the kinetic correlation effects between the vacancy and the solute are only approximated in Le Claire's model. The large differences in migration barriers in these systems prevent us from measuring diffusivities out of atomic kinetic Monte Carlo simulations because of kinetic trapping issues. The self-consistent mean field method (SCMF) is a promising path to provide kinetic properties for complicated systems. First developed for vacancy-mediated diffusion in bcc lattices [29], it has since then been extended to various structures [30–33] and migration mechanisms [34–36]. Basically, the SCMF method uses linear response theory to compute the flux resulting from a uniform driving force, which allows for identification of the Onsager matrix. It is based on a microscopic master equation, and thus provides a general way to link atomic-scale information (atomic jump frequencies) to macroscopic transport coefficients. In the framework of the thermodynamics of irreversible processes, transport coefficients relate chemical species fluxes to chemical potential gradients, which are the driving forces for diffusion. The Onsager matrix containing the transport coefficients is an n^2 matrix, where n is the number of species in the system. The diagonal coefficients can be related to diffusion coefficients in the dilute limit, while the off-diagonal coefficients dictate the flux coupling phenomenon which is responsible for effects such as radiation-induced segregation [37] and radiation-induced precipitation [38,39].

In this paper, we combine two state-of-the-art methods (DFT $+ U +$ OMC and SCMF) to get an accurate description of the vacancy-mediated migration of Kr and Xe in UN. We first introduce the aforementioned methods in Sec. II. Then, we present the energetic calculations (incorporation, binding, and migration) in Sec. III A, followed by a detailed study of solute transport coefficients and migration mechanisms in Sec. III B. A comparison with available experimental solute diffusivities is provided in Sec. III C. Finally, Sec. IV shows the impact of various model parameters on the computed kinetic properties.

II. METHODS

A. Density functional theory calculations

All DFT calculations in this paper have been performed using the Vienna *ab initio* simulation package (VASP). To handle correctly the strong correlation of the $5f$ electrons, the Liechtenstein implementation of the Hubbard correlation [5] is used, and the introduced metastable states, demonstrated to exist in a previous study [12], are handled with the occupation matrix control (OMC) scheme [10]. U and J were taken to be, respectively, 2.0 and 0.1 eV [11,12,40]. Wave functions were described using the projector augmented wave method [41]. The exchange-correlation functional chosen was the general gradient approximation with the PBE parametrization [42]. The potentials were taken from VASP database, treating 14 and 5 electrons as valence for, respectively, uranium and nitrogen. Xenon and krypton have 8 valence electrons. The cutoff energy has been set to 600 eV, although this high value was not needed for the elements studied here. This was done to have calculations consistent with systems containing oxygen (which requires a large cutoff energy) that are the focus of ongoing work. To account for elastic interactions between periodic images of the supercell, we use the correction introduced by Varvenne *et al.* [43] in the calculation of incorporation energies.

The supercell contains a rocksalt structure, which consists of two interpenetrating face centered cubic (fcc) lattices, one occupied by U atoms, and the other by N atoms. It has been shown that this structure presents antiferromagnetic (AFM) ordering and the exact structure used in our study was reported in Ref. [12]. This magnetic ordering is stable up to 53 K [44]. The structure is depicted in Fig. 1.

To calculate the kinetic coefficients of solutes, one first needs to know where these solutes are most likely to be located in the crystal. Therefore, the first step is to look at the solution energy of these solutes in different crystal positions. Here, four positions are investigated, for both Xe and Kr solutes: as substitutional atoms in the uranium and nitrogen sites, in the center of a Schottky defect and as an interstitial atom. These positions are shown in Fig. 2.

The solution energy of a solute is calculated as the sum of the formation energy of a defect and of the incorporation energy of the impurity in this defect:

$$E_{\mathrm{sol}} = E_{\mathrm{f}} + E_{\mathrm{inc}}. \tag{1}$$

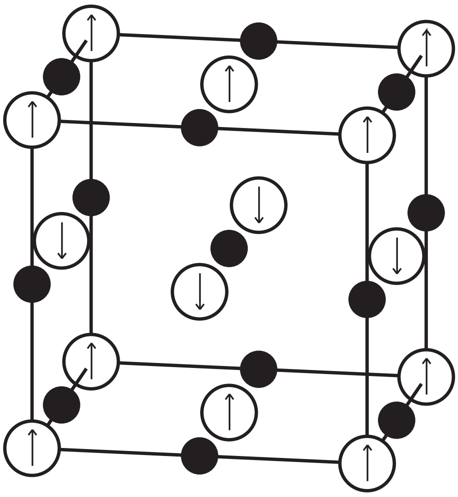

FIG. 1. Uranium nitride in the antiferromagnetic rocksalt structure. White: uranium atoms, black: nitrogen atoms. Spin orientations are represented by arrows.

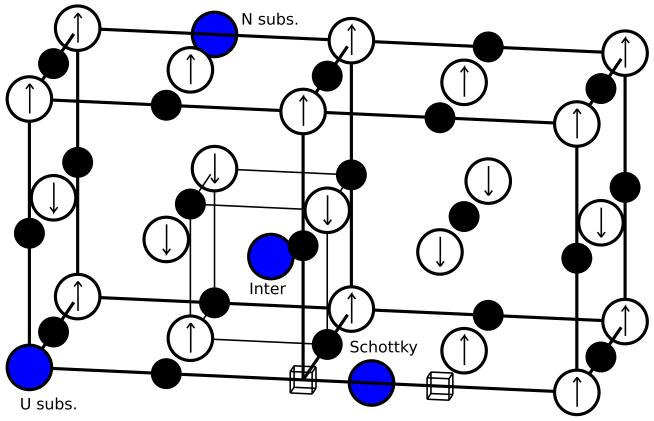

FIG. 2. Four possible positions for Xe and Kr solutes in UN: substitutional position on a uranium site, substitutional position on a nitrogen site, interstitial position, and center of Schottky defect.

Formation energies are not calculated in this study, but taken from Ref. [15].

The incorporation energies of xenon and krypton, presented in a previous paper [12], have been recalculated with a higher k-point density to make sure the system was well converged. For these simulations, the reference supercell for the incorporation energy calculations contained 32 atoms of each type. The k-point discretization has been increased from $2 \times 2 \times 2$ to $5 \times 5 \times 5$. The energies are converged to less than 1 meV/atom with respect to the k-point density.

For the binding and migration energy simulations, the reference cell was made larger, containing 108 atoms of each type, in order to avoid boundary effects. The energy convergence was set at 10 meV per atom. The k-point discretization was chosen to be $2 \times 2 \times 2$, to keep a k-point density similar to the one used to calculate the incorporation energies. The binding energy was calculated following Eq. (2), yielding a positive value when there was attraction and a negative value otherwise:

$$E_{\mathrm{b}} = E_{\mathrm{defect}} + E_{\mathrm{solute}} - E_{\mathrm{defect+solute}} - E_{\mathrm{ref}}, \qquad (2)$$

where $E_{\mathrm{defect+solute}}$ is the total energy of the system with the defect and the solute which binding energy we are investigating, E_{ref} is the energy of the supercell without defect, and E_{defect} and E_{solute} are the energy of the supercells with either the defect or the solute.

Migration energies are computed using the nudged elastic band [45] method as implemented in VASP with a spring constant of 5 eV/$\mathring{\mathrm{A}}^2$.

B. Self-consistent mean field method

The self-consistent mean field (SCMF) method uses linear response theory to compute a flux of species in response to a driving force, here a chemical potential gradient. It is derived from a microscopic master equation and thus provides a general way to obtain transport coefficients from a set of atomic jump rates. In the framework of the thermodynamics of irreversible processes, transport coefficients relate fluxes to driving forces

$$\begin{pmatrix} J_V \\ J_S \end{pmatrix} = -\begin{pmatrix} L_{VV} & L_{VS} \\ L_{SV} & L_{SS} \end{pmatrix} \begin{pmatrix} \frac{\nabla\mu_V}{k_B T} \\ \frac{\nabla\mu_S}{k_B T} \end{pmatrix}, \qquad (3)$$

where J_V and J_S denote the flux of vacancies and solutes, respectively, $L_{VV}, L_{VS} = L_{SV}$ and L_{SS} are the transport coefficients, $\nabla\mu_V$ and $\nabla\mu_S$ are the chemical potential gradient for each species, k_B is the Boltzmann constant, and T is the temperature. Note that all of these quantities are related to a particular direction.

In this study we apply the SCMF to compute transport coefficients for vacancy-mediated solute diffusion in antiferromagnetic rocksalt UN. Solutes Kr and Xe are more stable on the U sublattice (fcc), it is thus assumed that they diffuse on this sublattice only. Because of the AFM ordering, the diffusion network has the same symmetry as a tetragonally strained fcc cell. The SCMF equations have already been used for such system [31] and are identical to the one derived for isotropic systems. The difference resides in the application of these equations, and the proper identification of jump rates tangential to spin planes (T direction) and jump rates normal to spin planes (N direction). Below we provide the SCMF equations for the flux of vacancies in dilute alloys, and their derivation can be found in previous references (e.g., [36]). The flux of solute S is obtained by inverting V (vacancy) and S and taking into account the fact that the exchange rate between solute S and host atom h is always zero. The projected microscopic flux between sites i and s along the chemical potential gradient direction is

$$\begin{aligned} -J^V_{i\to s} &= \left\langle n^V_i n^\alpha_s \omega^{V\alpha}_{is} \frac{\vec{is}\cdot\vec{\nabla}(\mu_V - \mu_\alpha)}{k_B T} \right\rangle^{(0)} \\ &\quad + \left\langle n^V_i n^\alpha_s \omega^{V\alpha}_{is} \sum_k n^S_k \frac{\xi^{VS}_{ik} - \xi^{VS}_{sk}}{k_B T} \right\rangle^{(0)}, \end{aligned} \qquad (4)$$

where $\alpha \in \{S,h\}, n^\gamma_i$ is a site occupation number, and is equal to 1 if site i is occupied by species γ, and 0 if not. $\omega^{V\alpha}_{is}$ is the jump rate corresponding to the exchange between V at site i and species α at site s. ξ^{VS}_{ik} denotes the effective interaction between V at site i and S at site k. These interactions account for the deviation from the equilibrium system, and provide a quantitative estimation of kinetic correlation effects. Steady-state values for these interactions are obtained by solving a linear system containing one of the following equations for each effective interaction ξ^{VS}_{ij}:

$$\begin{aligned} &-\left\langle n^V_i n^S_j n^\alpha_s \omega^{V\alpha}_{is} \frac{\vec{is}\cdot\vec{\nabla}(\mu_V - \mu_\alpha)}{k_B T} \right\rangle^{(0)} \\ &\quad = \left\langle n^V_i n^S_j n^\alpha_s \omega^{V\alpha}_{is} \sum_k n^S_k \frac{\xi^{VS}_{ik} - \xi^{VS}_{sk}}{k_B T} \right\rangle^{(0)}. \end{aligned} \qquad (5)$$

In both equations, $\langle \ldots \rangle^{(0)}$ denotes the ensemble average over all possible configurations of the system using the equilibrium probability of each configuration as the weight function.

Equations (4) and (5) use an effective pair interaction Hamiltonian. In this framework, the accuracy of the calculation is controlled by the range R_{kin} of effective pair interactions, which is greater than the range of thermodynamic interactions. Unless specified otherwise, all calculations in this paper use $R_{\mathrm{kin}} = 2.5a$, where a denotes the lattice parameter. The convergence of the results with respect to this parameter is discussed in Sec. IV.

We follow previous developments for dilute systems and write transport coefficients as a sum of cluster transport coefficients weighted by cluster volumetric concentrations [36]. In a dilute system, it is assumed that when a vacancy meets a solute atom to form a pair they will have time to reach a local thermodynamic equilibrium between their various microscopic configurations before another vacancy or solute meets the pair. Hence, the kinetic properties of a VX pair cluster are identical to those which would be obtained in an infinitely dilute system and the Onsager matrix can be broken into cluster contributions that are independent of one another. In the dilute system under study, there are only three possible clusters (higher-order clusters being neglected because the probability that they form is small): the isolated vacancy, the vacancy-solute pair, and the isolated solute. The latter being immobile, it does not participate to transport coefficients. Furthermore, each cluster transport coefficient is split into two contributions: the mobility M, a scalar which is nothing but the diffusivity of a cluster treated as an isolated indivisible object, and the association/dissociation contribution AD, which contains the contribution of cluster association and dissociation to the global transport coefficients. Obviously, the isolated vacancy cannot dissociate so we are left with three contributions: vacancy mobility $M(V)$, vacancy-solute pair mobility $M(VS)$, and vacancy-solute pair association/dissociation contribution $AD(VS)$:

$$\begin{pmatrix} L_{VV} & L_{VS} \\ L_{SV} & L_{SS} \end{pmatrix} = [V]M(V)\begin{pmatrix} 1 & 0 \\ 0 & 0 \end{pmatrix} + [VS]M(VS)\begin{pmatrix} 1 & 1 \\ 1 & 1 \end{pmatrix} + [VS]\begin{pmatrix} AD(VS)_{VV} & AD(VS)_{VS} \\ AD(VS)_{SV} & AD(VS)_{SS} \end{pmatrix}. \tag{6}$$

$[V]$ and $[VS]$ denote the volumetric concentrations of isolated vacancies and vacancy-solute pairs, respectively. The main advantage of writing things this way is that cluster transport coefficients are intrinsic equilibrium properties of each cluster, and it is not assumed beforehand that cluster populations obey local equilibrium. Clusters with highly attractive binding energies do not dissociate often, which can lead to $AD(VS)_{\alpha\beta} \ll M(VS)(\alpha,\beta \in \{V,S\})$. It is the case in our system (VXe and VKr migration on the U sublattice of UN), so most of our discussion will be focused on mobilities. Because there are two nonequivalent directions in our system (T and N), all of the above cluster contributions will be calculated in each of these directions. Note that in the dilute limit

$$\lim_{[S]\to 0} L_{SS} = ([S] + [VS])D_S^*, \tag{7}$$

where $[S]$ is the volumetric concentration of isolated solutes, and D_S^* is the solute tracer diffusion coefficient, simply called solute diffusivity. Assuming $AD(VS)_{\alpha\beta} \ll M(VS)$, then $L_{SS} \simeq [VS]M(VS)$ such that

$$M(VS) \simeq \left(1 + \frac{[S]}{[VS]}\right) D_S^*. \tag{8}$$

It must be kept in mind that $M(VS)$ is an intrinsic property of VS clusters, while D_S^* is an averaged solute property which depends on the relative proportions between isolated solutes and VS pairs.

III. RESULTS

A. Energetics of the system

To access diffusion properties, a careful parametrization of the energetics of the system has to be carried out. We evaluate the incorporation energy of solutes in different defects and compute the vacancy-solute binding energy, as well as vacancy migration energies, either when it exchanges position with the impurity or with a uranium atom in the vicinity of the impurity.

1. Solution energies

The solution energy of Xe and Kr in UN has been computed in four different crystallographic positions, as shown in Fig. 2. The gas atoms have been set in substitutional positions, either located on a uranium or a nitrogen site. They have also been put in a tetrahedral interstitial position and in a Schottky defect. Due to the limited size of the supercell, a correction for elastic interactions between periodic images has been applied [43]. One can notice that the results are only slightly different (less than 2%) compared with those of our previous publication [12] which is due to the fact that we increased the k-point density.

The results are reported in Table I and although both Xe and Kr are found more stable in a Schottky defect if all types of defects are already present, the formation energy of such defect has been calculated to be very high [15], and for the present diffusion study, we focus on the substitutional uranium since the solution energy is the lowest for both solutes. One can also notice that the interstitial position, that seemed very unlikely from the incorporation energy, becomes more likely than the substitutional N and the Schottky defect positions when formation energies are taken into account.

2. Binding energies

To calculate the interaction range of the considered gas atoms with a vacancy, the binding energy has been computed.

TABLE I. Incorporation and solution energies (eV) of fission products in UN, without and with elastic correction [43]. Most stable configurations are in bold font.

Position	Subst. U	Subst. N	Schottky	Interstit.
E_{inc}(Kr)	2.87	6.26	**2.17**	11.54
Corrected value	2.75	5.91	**2.08**	10.59
E_{inc}(Xe)	3.76	8.60	**2.78**	14.62
Corrected value	3.59	7.89	**2.65**	13.09
E_{f} defect [15]	6.89	7.81	13.81	0
E_{sol}(Kr)	**9.64**	13.72	15.89	10.59
E_{sol}(Xe)	**10.48**	15.70	16.46	13.09

Here, several things have to be taken into account. For a given distance, the symmetry is broken by the spin planes. For instance, two atoms in third-nearest-neighbor (3NN) position can have the same or an opposed spin. Even when the spins are oriented in the same direction, there exist two 3NN configurations that are not symmetrically equivalent. Another example is the case of the second and fourth nearest neighbor (4NN), which are always between sites with spins oriented in the same directions. Thus, these configurations can be either normal to the spin plane (N configuration) or tangential to the spin plane (T configuration). To distinguish between these, we will use subscripts T or N.

All the configurations up to the eighth nearest neighbor (8NN) are represented in Fig. 3, and their binding energies are reported in Table II. One can see that the AFM ordered fcc lattice has the same symmetry as a tetragonal fcc cell. Unlike previous studies [18], we take into account the symmetry breaking due to the magnetic ordering, which produces additional nonequivalent configurations and transitions among them.

Due to the supercell size and boundary conditions, the 5NN and the 7NN positions are in a plane median between two solute atoms. The 8NN is the same as the 2NN. Therefore, the binding energy results for 5NN and 7NN are to be taken with caution because the imposed symmetry does not allow for proper relaxation of the configuration. For this reason, the normal and tangential positions have not been investigated for neighbors beyond the 4NN configuration.

Binding energies are very low beyond the 2NN position (less than 0.11 eV in absolute value), with the exception of the 5NN and 7NN interactions that we discussed. There is also a clear impact of the spin, that hints towards an anisotropy of the diffusion process. The interaction, be it attraction or repulsion, is stronger when the two atoms replaced by a vacancy and a solute are not in the same spin plane.

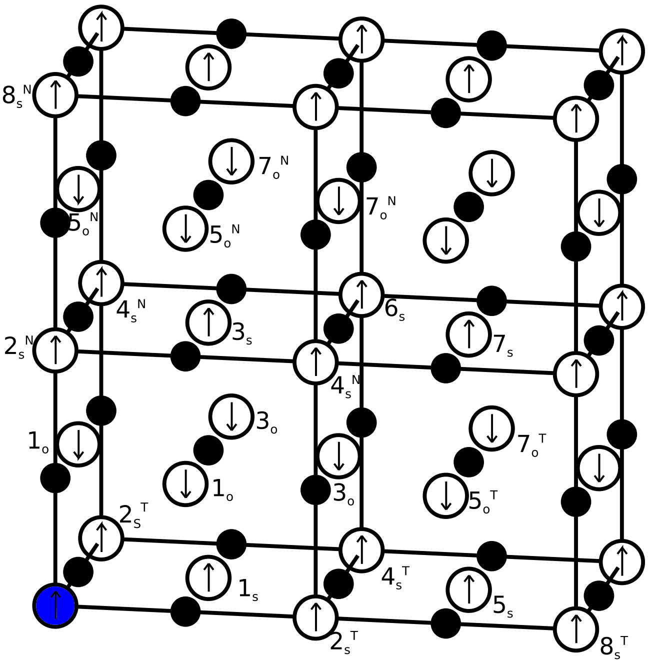

FIG. 3. Nearest-neighbor (NN) positions with respect to the solute (blue atom in the bottom left corner) in AFM-UN. "O" stands for opposite spins, "S" stands for same spin. When these subscripts are not sufficient to distinguish symmetrically inequivalent configurations, we use superscripts N (stands for normal) and T (stands for tangential) (see text).

TABLE II. Binding energy (eV) of V with either Xe or Kr in UN. A positive value indicates an attraction, and a negative one a repulsion. The configurations are pictured in Fig. 3.

Configuration	Name	E_b (VXe)	E_b (VKr)
1 NN same	1_S	0.74	0.90
1 NN opposed	1_O	0.95	1.04
2 NN same tangential	2_S^T	−0.39	−0.19
2 NN same normal	2_S^N	−0.46	−0.20
3 NN same	3_S	−0.03	0.04
3 NN opposed	3_O	0.03	0.11
4 NN same tangential	4_S^T	−0.04	0.01
4 NN same normal	4_S^N	0.02	0.06
5 NN same	5_S	0.33	0.43
5 NN opposed tangential	5_O^T	0.23	0.23
5 NN opposed normal	5_O^N	−0.03	0.00
6 NN same	6_S	−0.06	0.03
7 NN same	7_S	−0.11	0.09
7 NN opposed	7_O	0.59	0.08

For both Xe and Kr, the very strong attraction with the vacancy when located in a 1NN configuration can be explained by the fact that the gas atom relaxes strongly towards the vacancy. Because of this movement of the solute towards the vacancy, between 20% and 30% (depending on the spin and the species) of the way to the saddle point is covered, the stresses created by the incorporation of the gas atom in the bulk system are greatly relaxed. For the 2NN configuration, the gas atom relaxes away from the vacancy, whereas the uranium atoms that are 2NN of the vacancy relax towards it. In particular, the uranium atoms in 1NN position with respect to the vacancy relax towards it by 3%–5% of the distance to the saddle point, which breaks the symmetry around the gas atom, without giving it much more space. The effect on nitrogen atoms is also peculiar since the one between the vacancy and the solute strongly relaxes towards the vacancy (about 8%), whereas the other five N atoms around the vacancy move away, as in the bulk system with only one vacancy on a uranium site. The presence of the nitrogen atom in-between the vacancy and a 2NN solute atom probably explains the negative binding energies (repulsion) of the 2NN configurations.

3. *Migration energies*

In this study, we consider only vacancy-assisted migration. As discussed earlier, our goal is to check the impact of both the distance threshold chosen for the interaction between the vacancy and the gas atom, and the effect of magnetic ordering which might lead to anisotropic diffusion. To do that, the migration energies of all the possible jumps involving the solute and the 1NN and 2NN uranium atoms are computed. The resulting jump network is represented in Fig. 4.

Migration energy values shown in Table III are for the migration from the first to the second position, tracking the

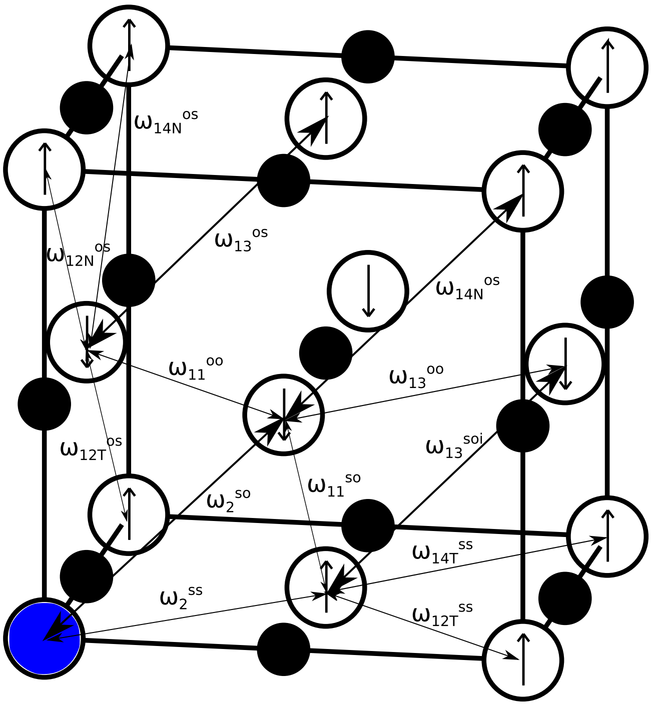

FIG. 4. Considered transitions. The lower script represents the distances of the initial and final positions of the vacancy when compared to the solute. The upper script represents the spin orientation of the initial and final sites occupied by a vacancy, with respect to the solute.

displacement of the vacancy. The values in parentheses have to be added to get the migration energy from the second position to the first one. Also reported in Table III are the saddle-point energies. The highest saddle-point energy in a migration path defines the rate-limiting step of this path. This point is discussed further in the next section. With our binding energy convention,

$$E_{sp} = E_m - E_b \tag{9}$$

Vacancy-solute exchange energies are much lower than the other ones, both for Xe and Kr. As discussed in the previous section, the equilibrium position of gas solutes is strongly relaxed towards the vacancy and 20% to 30% of the path to the saddle-point position is already done, which is likely to be the reason for such a low migration energy. As a consequence, we expect this jump to occur very frequently, but since it alone cannot produce long-range diffusion, it will most likely be a highly correlated jump, and diffusion will be limited by surrounding jumps. The migration energies of all these jumps are much higher, and take values in a wide range of energies (more than 1.5-eV difference). In particular, looking at the possibilities for the vacancy to jump from a 1NN position to another position, which is required for long-range diffusion, the migration energies can be as low as 2.78 eV and as high as 3.87 eV. With regards to the previous discussion on the relaxation of the xenon and krypton atom towards the vacancy when they are in a 1NN configuration, it is worth noting that at the saddle point of the ω_{11} transitions, the solute atom is back to the perfect lattice site. Indeed, at this point, the distance between the solute and the migrating uranium atom is the shortest, and if the gas atom had stayed where it was, the migration energy would be much higher. The high value of the ω_{11} migration energies (compared to the ω_2 migration energies) is a consequence of the necessary destabilization of the solute atom. These observations motivate the need for a complete kinetic model able to perform the statistical average of all possible jumps and identify the main migration path. This will be the topic of Sec. III B.

TABLE III. Migration energy of Xe and Kr in UN, in eV. "Ini" corresponds to the initial position of the vacancy and "Fin" to the final one. The transitions are represented in Fig. 4. The transitions ω_2 involve a displacement of the solute, and for this reason, the initial and final positions of the vacancy for the transition ω_2^{SO} are the same, although there is a change of spin plane. Saddle-point energies E_{sp} are computed in Eq. (9).

Ini	Fin	Trans	E_m (Xe)	E_m (Kr)	E_{sp} (Xe)	E_{sp} (Kr)
1_S	1_S	ω_2^{SS}	0.95 (+0.00)	0.55 (+0.00)	0.21	−0.35
1_O	1_O	ω_2^{SO}	0.83 (+0.00)	0.47 (+0.00)	−0.12	−0.57
1_O	1_O	ω_{11}^{OO}	3.28 (+0.00)	3.18 (+0.00)	2.33	2.14
1_S	1_O	ω_{11}^{SO}	2.78 (+0.21)	2.74 (+0.14)	2.04	1.84
1_S	2_S	ω_{12}^{SS}	3.71 (–1.13)	3.67 (–1.09)	2.97	2.77
1_O	2_S^T	$\omega_{12^T}^{OS}$	3.87 (–1.34)	3.69 (–1.23)	2.92	2.65
1_O	2_S^N	$\omega_{12^N}^{OS}$	3.80 (–1.41)	3.53 (–1.24)	2.85	2.49
1_S	3_O	ω_{13}^{SO}	3.09 (–0.72)	3.14 (–0.79)	2.35	2.24
1_O	3_S	ω_{13}^{OS}	3.22 (–0.98)	3.16 (–1.01)	2.27	2.12
1_O	3_O	ω_{13}^{OO}	3.52 (–0.92)	3.29 (–0.93)	2.57	2.25
1_S	4_S	ω_{14}^{SS}	3.36 (–0.78)	3.39 (–0.89)	2.62	2.49
1_O	4_S^N	$\omega_{14^N}^{OS}$	2.91 (–0.93)	2.94 (–0.99)	1.96	1.90
2_S^N	3_S	$\omega_{2^N3}^{SS}$	2.21 (+0.44)	2.59 (+0.24)	2.67	2.79
2_S^T	3_O	$\omega_{2^T3}^{SO}$	2.39 (+0.41)	2.56 (+0.29)	2.78	2.75
2_S^T	5_S	$\omega_{2^T5}^{SS}$	3.08 (+0.72)	3.10 (+0.62)	3.47	3.29
2_S^T	5_O^T	$\omega_{2^T5^T}^{SO}$	2.79 (+0.62)	2.82 (+0.42)	3.18	3.01
∞	∞	ω_0^{SS}	3.31 (+0.00)	3.31 (+0.00)	3.31	3.31
∞	∞	ω_0^{SO}	3.63 (+0.00)	3.63 (+0.00)	3.63	3.63

B. Transport coefficients

In this section, we combine the DFT values of migration and binding energies (Sec. III A) with the SCMF method to compute vacancy-solute (VS, $S \in \{\mathrm{Xe,Kr}\}$) pair transport coefficients. These cluster transport coefficients provide insight into the migration mechanism of VS pairs at the atomic scale. Binding energies are considered up to the 6NN, and all jump frequencies that were computed are used in the calculations (Table III). Of course, this DFT-computed set of migration barriers is not exhaustive, and all missing migration barriers needed as input in the SCMF formalism (mainly dissociation frequencies) are obtained via the commonly used kinetically resolved activation (KRA) barrier approximation [46,47]

$$E_m(1 \rightarrow 2) = \frac{E_b(1) - E_b(2)}{2} + Q, \tag{10}$$

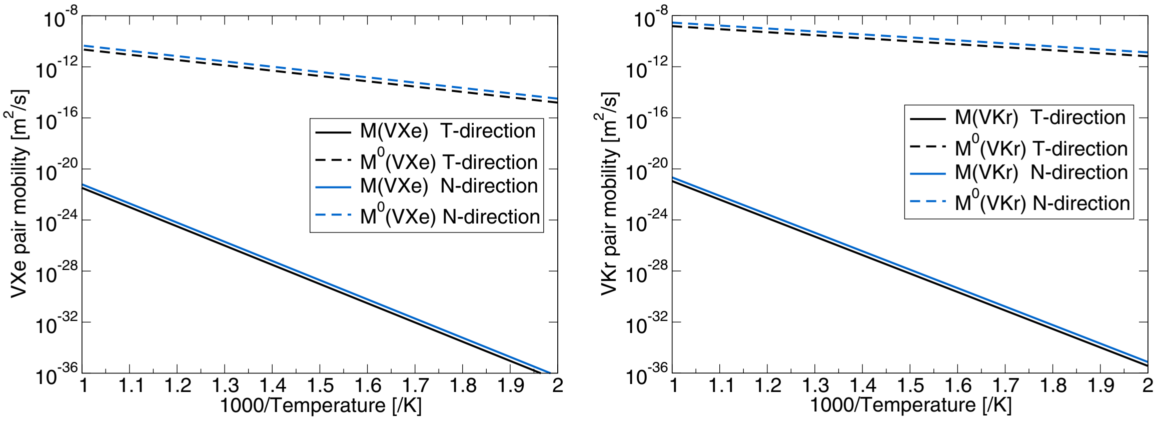

FIG. 5. Uncorrelated mobilities M^0 (dashed lines) and correlated mobilities M (solid lines) for VXe pairs (left plot) and VKr pairs (right plot). On both of these plots, blue lines correspond to diffusion in the N direction while black lines correspond to diffusion in any T direction.

where $E_m(1 \rightarrow 2)$ is the migration energy between states 1 and 2, $E_b(k)$ is the binding energy of state k, and Q is a constant value chosen as the bulk vacancy migration energy. Note that in our systems, there are two possible Q values depending on whether the jump is along the T or N direction. All jump attempt frequencies are set to the Debye frequency $\nu_0 = 23.8$ THz [48]. Because all attempt frequencies are identical in our calculation, cluster transport coefficients are proportional to ν_0. The effect of considering various attempt frequencies for various jump rates will be addressed in Sec. IV.

Figure 5 shows VS pair mobilities ($S \in \{\text{Xe,Kr}\}$) as a function of the inverse temperature. These mobilities were computed in both T and N directions. For both VS pairs, the difference between T and N diffusion is small [$M(VS)_N \simeq 2M(VS)_T$] and does not vary much with temperature. The fact that mobilities $M(VS)$ show an Arrhenius behavior over the whole temperature range demonstrates that there exists one energetically favored migration path. Moreover, the small diffusion anisotropy indicates that the energy landscape of the main migration path is similar in all directions. Figure 5 also shows the uncorrelated mobilities $M^0(VS)$. When kinetic correlations are ignored [all effective interactions set to zero in Eq. (4)], the computation of transport coefficients reduces to a thermodynamic average of all possible jump rates in the system. For Kr and Xe diffusion in UN, the exchange between vacancy and solutes has a much lower migration energy than any other barrier in the system (cf. Table III). Thus, the corresponding rate will dominate the thermodynamic average of jump rates, and the resulting estimation of transport coefficients will be high (dashed lines in Fig. 5). But, these exchange jumps alone do not provide long-range diffusion. For that to happen, the vacancy also needs to be able to migrate around the solute in-between two exchange jumps. The exchange jump rate being orders of magnitude higher than these vacancy jumps around the solutes, there will be many exchange jumps before a single jump of the vacancy around the solute. These successive exchange jumps do not produce any net diffusion of the VS pair, hence, the important difference between correlated and uncorrelated transport coefficients in Fig. 5 (about 12 orders of magnitude at $T = 1000$ K). Generally speaking, these plots demonstrate the importance of computing correlation effects to evaluate solute diffusivities.

Usually, high binding energy between vacancies and solute is associated with vacancy trapping and immobile vacancy-solute pairs [49–52]. If one assumes the saddle-point energy as nearly independent of local atomic configurations, then high VS binding will produce a deep well from which it is difficult to escape. The reality is that saddle-point energies do depend on local atomic configurations. It is thus highly speculative to predict beforehand what will be the effect of a solute on the average vacancy diffusivity. In our system, the 1NN V-S binding is very high (between 0.74 and 1.04 eV, cf. Table II), so one could expect solutes to trap vacancies. But, it turns out that solutes also locally lower the vacancy saddle-point energies: careful inspection of Table III reveals that for any computed vacancy jump in the neighborhood of the solute, saddle-point energies are lower than bulk saddle-point energies. To summarize, solutes will indeed trap vacancies in the sense that vacancies will hardly dissociate from solutes, but the resulting VS pairs are far from immobile, and Fig. 6 shows that VS are indeed more mobile than isolated vacancies. Thus, for a given vacancy concentration, increasing the concentration of Xe and Kr in UN leads to an increased vacancy diffusivity. From a qualitative point of view, it is interesting to note that VS pairs diffuse faster in the N direction than in the T direction, whereas it is the opposite for isolated vacancies. Also, the diffusion anisotropy is more important for isolated vacancies than it is for VS pairs, especially at low temperature. All curves in Fig. 6 have been fitted with an Arrhenius expression $M(\alpha) = D_0 \exp(-E_m/k_BT)$, where D_0 is a diffusion prefactor, and E_m the effective migration energy associated with the migration of cluster α. Fitted parameters are given in Table IV.

The fact that the Arrhenius fit is valid across the whole temperature range indicates that for each cluster there is a single migration mechanism responsible for the long-range diffusion of this cluster, which is explained in Fig. 7. The effective migration barrier corresponding to a given jump sequence can be estimated from the "highest barrier approximation" [53]. In this framework, the effective migration barrier of the diffusion

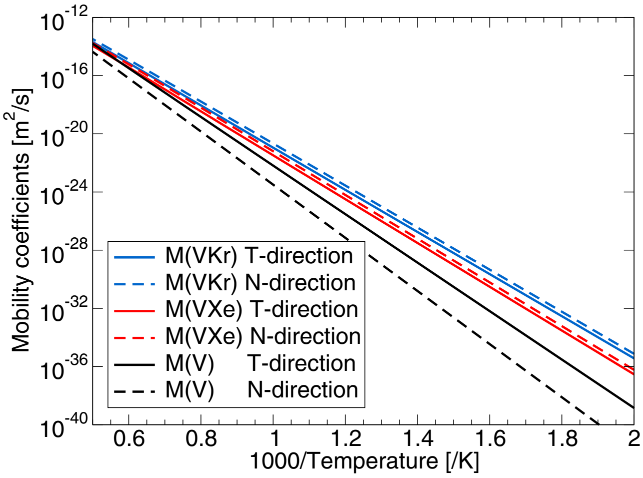

FIG. 6. Cluster mobilities M as a function of the inverse temperature for three clusters: isolated vacancy (black lines), VXe pairs (red lines), and VKr pairs (blue lines). For each of these clusters, two mobilities are shown, one associated with diffusion in the N direction (dashed lines) and the other associated with diffusion in the T direction (solid lines).

path is the energy difference between the highest saddle-point configuration of the path and the most stable configuration. In both cases under study, the most stable configuration of the VS pair is the 1NN opposite configuration (cf. Table II), with a binding energy of 0.95 and 1.04 eV for Xe and Kr, respectively. Then, we are looking for a jump sequence that translates the initial VS configuration, either in the T or N direction. Among these jump sequences, the most probable one will be the one with the lowest saddle-point energy, where the saddle-point energy of a jump sequence is defined as the highest saddle-point energy among each of the individual jumps in the jump sequence. Applying this method, we identify the most probable long-range diffusion mechanisms for VS pairs (which are similar for each solute) in both nonequivalent directions (Fig. 7). The idea is to perform out-of-plane jumps only because they have smaller saddle-point energies than in-plane jumps (it is the opposite for an isolated vacancy). The solute-vacancy exchange has a low saddle-point energy so they will not be the rate-limiting step of this migration mechanism, which is the ω_{11}^{OS} jump for both cases (T and N diffusion), which explains the low anisotropy of VS pair mobility. It is interesting to point out that for diffusion in the T direction, it is more efficient to perform out-of-plane jumps. From a quantitative point of view, the effective migration energy of these jumps can be estimated with the highest approximation barrier and we find $E_m^{\text{eff}}(V\text{Xe}) = 0.95 + 2.04 = 2.99$ eV and $E_m^{\text{eff}}(V\text{Kr}) = 1.04 + 1.84 = 2.88$ eV, in good agreement with the fits in Table IV.

TABLE IV. Arrhenius fit of cluster mobilities plotted in Fig. 6.

	$M(\alpha)_{\text{T}}$		$M(\alpha)_{\text{N}}$	
	D_0 (m^2/s)	E_m (eV)	D_0 (m^2/s)	E_m (eV)
$\alpha = V$Xe	3.83e−7	2.99	6.08e−7	2.98
$\alpha = V$Kr	3.50e−7	2.88	5.80e−7	2.87
$\alpha = V$	3.18e−6	3.31	5.83e−6	3.63

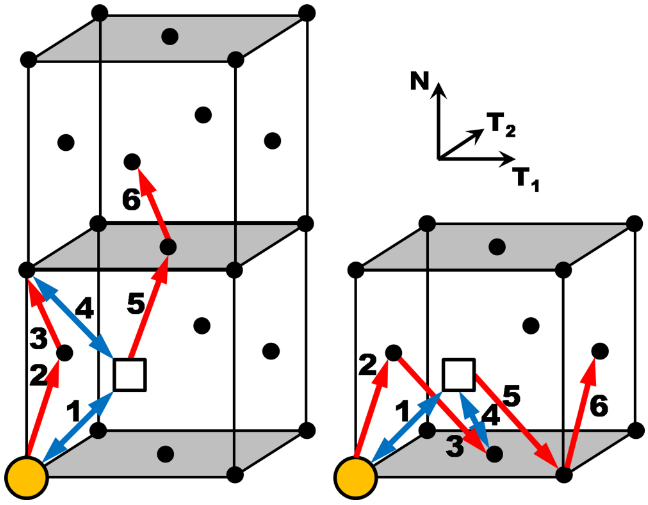

FIG. 7. Long-range diffusion mechanism for VS pairs. Left-hand (resp. right-hand) side shows diffusion in the N (resp. T) direction. The initial positions of S and V are depicted as a yellow sphere and white square, respectively. Black spheres show the AFM-fcc lattice of U atoms. Blue double-headed arrows denote a S-V exchange, while red single-headed arrows denote a U-V exchange. The number beside each arrow corresponds to the order in which these jumps proceed. The final position of S is obtained by following double-headed arrows, while the final position of V is at the sixth arrow head. Final and initial positions are thus equivalent.

In short, the AFM ordering breaks the symmetry of the fcc sublattice, which creates anisotropic binding and migration energies. Because of this anisotropy, the VS pair does not diffuse with the same migration mechanism in both T and N directions. But, both migration paths go through the exact same metastable and saddle-point states. Thus, there is essentially no macroscopic diffusion anisotropy for VS pairs.

Finally, it is interesting to look at cluster flux coupling coefficients for two reasons: First, these coefficients are very sensitive to the details of atomic migration, much more than the mobilities. Second, as long as these coefficients are close to unity, it means that $AD(VS) \ll M(VS)$, and that the diffusion properties of the system depend mainly on cluster mobilities. If it is not the case, then we also have to consider the association/dissociation terms (two coefficients) which are more complicated to discuss (see Ref. [36]). The cluster flux coupling ratios are defined as

$$\frac{L_{VS}(VS)}{L_{SS}(VS)} = \frac{M(VS) + AD_{VS}(VS)}{M(VS) + AD_{SS}(VS)}, \tag{11}$$

$$\frac{L_{SV}(VS)}{L_{VV}(VS)} = \frac{M(VS) + AD_{SV}(VS)}{M(VS) + AD_{VV}(VS)}. \tag{12}$$

The first flux coupling coefficient is commonly denoted as the drag ratio (it does not depend on the respective value of V and VS concentrations) and allows to predict radiation-induced segregation behavior (e.g., [33,54]). Both coefficients are shown for each solute and each direction in Fig. 8. Indeed, the flux coupling anisotropy (difference between solid and

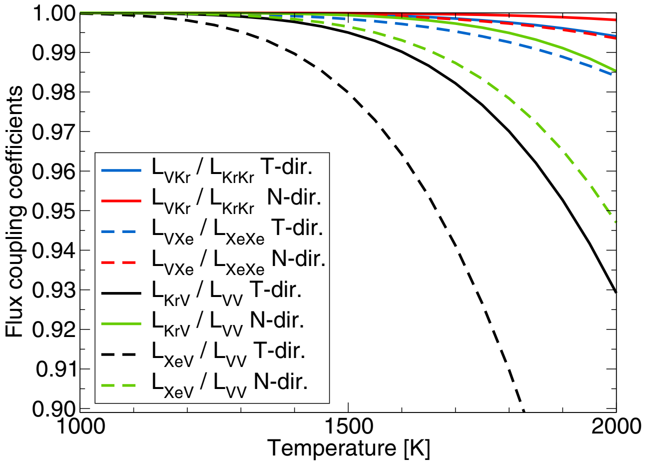

FIG. 8. VS pairs flux coupling coefficients as a function of temperature. A color is related to one type of cluster flux coupling coefficient [$L_{VS}(VS)/L_{SS}(VS)$ or $L_{SV}(VS)/L_{VV}(VS)$] in one particular direction (N or T), hence, the four different colors. Solid lines correspond to $S =$ Kr and dashed lines correspond to $S =$ Xe.

dashed curve of a given color) is more pronounced than for the mobility coefficients. All of these coefficients are exactly equal to unity below $T = 1000$ K, so at these temperatures diffusion of solutes is governed by the long-range migration of practically indivisible VS pairs. At higher temperature, the dissociation of these clusters starts to play a role, but still a minor role because the cluster flux coupling coefficient stays close to unity. Figure 8 also shows that flux coupling is always higher in the N direction than in the T direction.

If one knows the concentrations of isolated vacancies and vacancy-solute pairs, the second cluster flux coupling coefficient [Eq. (12)] can be turned into macroscopic flux coupling coefficients (which are commonly used in the framework of the thermodynamics of irreversible processes to study radiation-induced segregation) using Eq. (6):

$$\frac{L_{SV}}{L_{VV}} = \frac{M(VS) + AD(VS)_{SV}}{M(VS) + AD(VS)_{VV} + \frac{[V]}{[VS]}M(VS)}. \tag{13}$$

Note that the denominator of Eq. (13) is always positive, such that the pair flux coupling ratio [Eq. (12)] dictates the qualitative nature of the flux coupling phenomenon (either positive or negative).

C. Comparison with experimental data

It is difficult to make a relevant comparison of the solute diffusion coefficient with experimental data because solute diffusivity is proportional to the vacancy concentration in the system. Experimental measurements (gathered by Deforest [2]) are indirect measurements performed under irradiation where the vacancy concentration is unknown. Nevertheless, we are able to compute the equilibrium solute diffusivity using the thermal vacancy concentration. The solute diffusion coefficient D_S^* is expressed as

$$D_S^* = [V]ZM(VS), \tag{14}$$

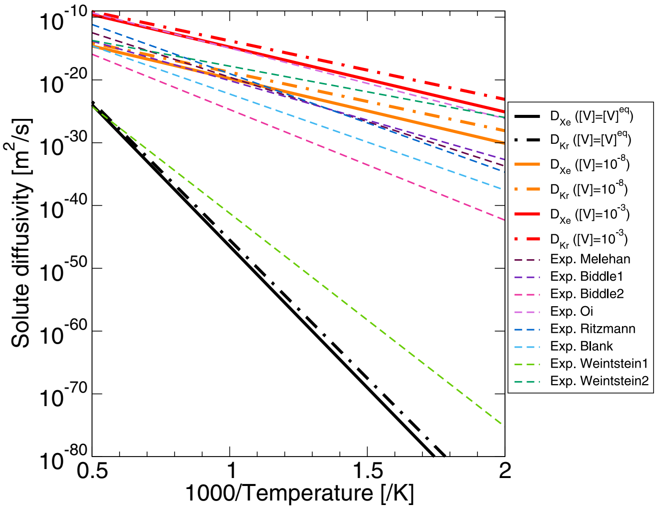

FIG. 9. Comparison between experimental measurements (as gathered in Ref. [2] for Xe and Kr) and our estimate of solute diffusivities for various vacancy concentrations. The diffusion anisotropy being small for both VXe and VKr pairs, we only show the diffusivity in the T direction. Melehan [57], Biddle 1 and 2 [58], Oi [59], Ritzmann [60], Blank [61], and Weinstein 1 and 2 [55,56]

where $[V]$ is the vacancy concentration, Z is the pair partition function (binding energy term), and $M(VS)$ is the mobility of the vacancy-solute pair. Under equilibrium conditions, the vacancy concentration reads as

$$[V]^{\mathrm{eq}} = \exp\left(-\frac{E_f(V)}{k_B T}\right), \tag{15}$$

where $E_f(V)$ is the vacancy formation energy (cf. Table I).

Using Eqs. (14) and (15), we can plot four diffusion coefficients as each solute (Xe, Kr) have anisotropic diffusivity (T or N directions). As diffusion anisotropy is almost negligible in this system (see Fig. 6), we will only plot the diffusivity in the T direction for the sake of clarity in Fig. 9. The experimental data gathered in Ref. [2] are plotted as blue dashed lines. Most experimental measurements are orders of magnitude higher than our theoretical predictions at equilibrium (black lines). This is most likely a consequence of the fact that these measurements were performed on irradiated samples, for which the vacancy concentration is unknown, but probably orders of magnitude higher than the equilibrium vacancy concentration. It is interesting to note that there is one experimental result that gives very low values of diffusivity, in qualitative agreement with our theoretical prediction [55]. This measurement might be closer to equilibrium than the other ones, but it is most likely to be related to a modeling issue: the bubble contribution was not taken into account and a complete interconnection of the grain boundaries was assumed in Ref. [55], but in a subsequent study considering the action of the bubble, a diffusion coefficient closer to the other experiments was found [56].

Using Eq. (14), we computed solute diffusivity for two high-vacancy concentrations (independent of temperature): 10^{-3} and 10^{-8}. It seems that the calculations $[V] = 10^{-3}$ give the upper limit for experimental measurements, while the theoretical prediction for $[V] = 10^{-8}$ seems to be in-between various measurements. To go further, a more detailed description of these experiments would be needed, as well as a model of point-defect evolution under irradiation to estimate the vacancy concentration in the systems. The difference between experimental measurements and theoretical predictions of solute diffusivity can also stem from several other reasons:

(i) Only vacancy-mediated diffusion has been considered here. It is possible that the diffusion of gas atoms in UN happens following other more efficient diffusion mechanisms.

(ii) The experimental measurements are indirect (fission gas release rate) which requires a number of modeling assumption, which are not always the same [62,63], and the stoichiometry of the sample is not guaranteed.

(iii) Most of these measurements are performed at high temperature (where there is no AFM ordering of the UN structure) and then extrapolated to lower temperatures. Migration properties might thus be different at these temperatures, which questions the validity of the extrapolation.

IV. DISCUSSION: COMPARISON BETWEEN VARIOUS KINETIC MODELS

In this section, we will discuss various approximations of the kinetic model to test the robustness of the conclusions drawn from the previous section.

First, we look at the impact of the range of effective interactions R_{kin} on the drag ratio, chosen here because it is the most sensitive quantity to compute. Figure 10 shows the drag ratio obtained for the VXe pair (similar results are obtained for VKr pairs) for $2a \leqslant R_{\text{kin}} \leqslant 4a$, where a is the lattice parameter of the fcc cell. The range of thermodynamic interactions is $\sqrt{3}a$ (6NN) so it would not be consistent to set R_{kin} below this value. Figure 10 clearly shows that the drag ratio converges with increasing values of R_{kin}. Taking the drag ratio obtained for $R_{\text{kin}} = 4a$ as the reference value, the drag ratio is already converged up to a 0.3% error at $T = 2000$ K when $R_{\text{kin}} = 2.5a$. Thus, we chose this R_{kin} value as a good compromise between accuracy and computational time. All results in this paper, unless otherwise specified, are obtained with $R_{\text{kin}} = 2.5a$.

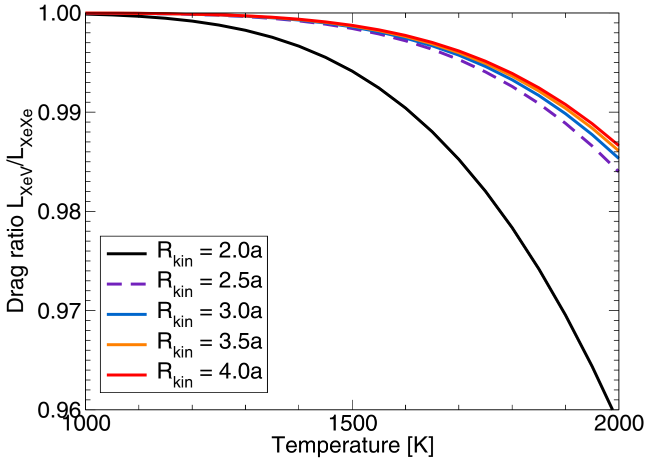

FIG. 10. Drag ratio for VXe pairs computed using the SCMF method with varying range of effective interactions (R_{kin}). The dashed line ($R_{\text{kin}} = 2.5a$) corresponds to the value chosen for the calculations in this study.

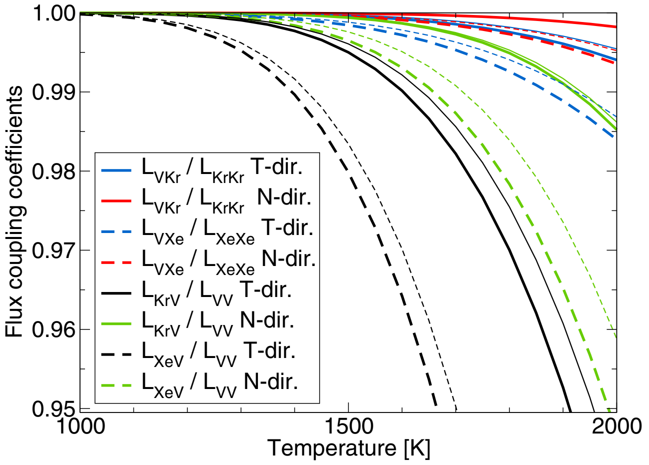

FIG. 11. The thick lines of this plot are exactly the same as those in Fig. 8. Thin lines are obtained using the 4NN thermodynamic model [meaning that 5NN and 6NN binding are set to zero, and migration barriers from or to this configuration are obtained using the KRA approximation, cf. Eq. (10)].

Next, we investigate the impact of 5NN and 6NN bindings on the transport coefficients. The reason is that, as explained in Sec. III A, the 5NN configuration is geometrically constrained by the size of the supercell used for DFT calculations. Hence, it is possible that the relaxation of these configurations is not complete, and the associated vacancy-solute binding energy inaccurate. Thus, we performed the SCMF calculations assuming that 5NN and 6NN configurations have a binding energy of zero, which we call the "4NN" thermodynamic model, whereas the full calculation is denoted as the "6NN" thermodynamic model. Migration barriers for jumps to and from these configurations are estimated using the KRA approximation [Eq. (10)]. These changes have a negligible impact on VS pair mobilities, which is expected as we have shown that the mobility of these clusters is fully controlled by 1NN configurations (Fig. 7). Thus, Fig. 11 compares 4NN and 6NN thermodynamic model on the pair flux coupling ratios, which is much more sensitive quantity than the mobilities. Thick lines correspond to the 6NN model (exact same results as in Fig. 8), while thin lines correspond to the 4NN model. Pair flux coupling coefficients are always higher in the latter thermodynamic model, but the difference is overall quite small, so it can be safely stated that 5NN and 6NN configurations do not affect the results of the previous section, and that the kinetic properties of VKr and VXe pairs are mostly insensitive to potential inaccuracies in the computed 5NN and 6NN binding energies.

In Fig. 7, we have shown that long-range migration of VXe and VKr pairs occurs via successive jumps in the 1NN shell. Now, we want to investigate the effect of the second to 6NN configurations (all taken into account in our calculations) on the overall mobility of the pair. For this purpose, we compute the mobility of VS pairs for a simplified model where the range of both thermodynamic and effective interactions are set to the 1NN distance $\sqrt{2}a$. The escape jump

TABLE V. Results of Arrhenius fits [diffusion prefactors D_0 in (10^7 m^2/s) and migration energies E_m in (eV)] to VS mobilities for various kinetic models. Data for the first two lines are obtained using the SCMF method with different thermodynamic and kinetic approximations (see text). Previous approximations of the diffusivity are used for comparison: Le Claire's model does not take into account the migration anisotropy in AFM fcc UN and Andersson's model does not compute kinetic correlations.

	$M(V\mathrm{Xe})_T$		$M(V\mathrm{Xe})_N$		$M(V\mathrm{Kr})_T$		$M(V\mathrm{Kr})_N$	
	D_0	E_m	D_0	E_m	D_0	E_m	D_0	E_m
$R_{\mathrm{kin}} = 2.5a$	3.83	2.99	6.08	2.98	3.50	2.88	5.80	2.87
$R_{\mathrm{kin}} = \sqrt{2}a$	3.62	2.99	6.31	2.97	3.32	2.88	5.85	2.87
Le Claire [65]	7.17	3.09	19.9	2.92	4.80	3.05	19.1	2.91
Andersson [66]	5.71	3.28	5.71	2.99	5.71	3.18	5.71	2.88

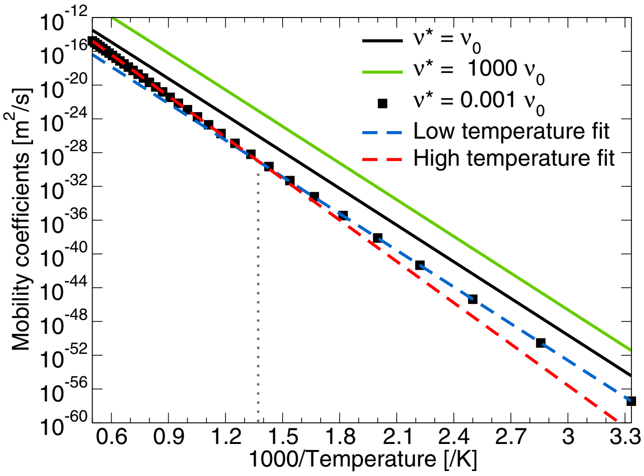

FIG. 12. Mobility of the VKr pair in the N direction plotted for various values of the attempt frequency of the ω_{11}^{SO} jump ($\nu*$). All other jump rates have an attempt frequency set to ν_0. When $\nu* = 0.001\nu_0$ (black squares), $M(V\mathrm{Kr})_N$ is not a straight line anymore, but it can be fitted by two Arrhenius expressions, one at low temperature (blue dashed line) and the other at high temperature (red dashed line). The crossover temperature between these indicates a change in the migration mechanism of the VKr pair.

rates from 1NN configurations are estimated with the KRA approximation [Eq. (10)]. The analytical expressions for such a model (also valid for a tetragonal fcc cell) are provided in the Appendix section. Table V shows the comparison between Arrhenius fits of VS mobilities in both N and T directions. The first line ($R_{\mathrm{kin}} = 2.5a$) corresponds to the full model (with thermodynamic interaction up to the 6NN) while the second line ($R_{\mathrm{kin}} = \sqrt{2}a$) is the 1NN only model we just described. These two models are in very good agreement, both for migration energies and diffusion prefactors, which again stresses the fact that only 1NN jumps are responsible for the long-range migration of the vacancy-solute pair, and that other configurations do not play a significant role. This is because the binding energy is much smaller (less attractive) than 1NN configurations, and most of the saddle-point energies of transitions between the second to 6NN states are high, which makes these jumps unlikely to occur.

We also compared these results to another model (third line of Table V) which is basically a Le Claire five-frequency model for fcc alloys [64,65], which does not take into account the diffusion anisotropy. In this model, thermodynamic and effective interaction are also limited to 1NN shells. For mobilities in the T direction, we used in-plane binding and migration energies as inputs to this model, while for mobilities in the N direction we used out-of-plane binding and migration energies. In both cases, the agreement is not as good as the 1NN SCMF ($R_{\mathrm{kin}} = \sqrt{2}a$) model. Diffusion prefactors and migration energies are higher with a Le Claire model compared to the SCMF reference, except for $M(V\mathrm{Xe})_N$ where the effective migration energy is a little bit smaller. Because of the jump-rate anisotropy, out-of-plane are much more probable than in-plane jumps, which changes the topology of the diffusion network compared to an isotropic fcc cell. Because this feature is not taken into account in the Le Claire approach, kinetic correlations are not evaluated properly, hence, the deviation observed in Table V. Compared to Le Claire's model, Andersson's model [66] does not account for kinetic correlations. The agreement with the full SCMF calculation is quite good for N direction, which is not surprising as we have explained that vacancy-mediated diffusion of Xe and Kr in UN basically reduces to one rate-limiting step, the jump of V around the solute, which is the core assumption of Andersson's model. Nevertheless, nothing guarantees the general validity of this assumption. In the T direction, migration energies are not well estimated with Andersson's model because the mechanism that is considered is not the most probable one.

Finally, we investigate the effect of jump prefactors on the mobility of VS pairs. Let us remind that up to now, all jump rates have the same attempt frequency, denoted as ν_0. According to transition state theory, the attempt frequency is a function of the mass of the jumping atom [67]. Hence, the expected first-order effect would be that the attempt frequency for vacancy-solute exchange should be different from the attempt frequency for vacancy-uranium atom exchange. Looking at Fig. 7, there are two jumps controlling the migration mechanism: V-S exchange ω_2^{OO} and V-U exchange ω_{11}^{OS} (related to ω_{11}^{SO} by detailed balance). The relative probability between these jumps is given by the saddle-point energy difference ΔE_{sp}, which is 2.16 eV for VXe pairs and 2.41 eV for VKr pairs (cf. Table III), and the V-U exchange is obviously the limiting step. Even at $T = 2000$ K, $\exp(\Delta E_{sp}/k_B T) \simeq 10^6$. The V-S exchange jump is so much faster than the V-U exchange jump that changing the attempt frequency of solute-vacancy exchange by less than six orders of magnitude (which is not reasonable) will not have much effect on the mobilities. Knowing that, we investigated the effect of the attempt frequency of the rate-limiting step ω_{11}^{OS}. This attempt frequency is denoted $\nu*$ in the discussion. Figure 12 shows the mobility coefficient of a VKr pair in the N direction. When $\nu*$ is set three orders of magnitude higher than all other attempt frequencies (ν_0), the mobility simply increases by the same quantity which is not surprising: the rate-limiting step becomes faster, so the whole mobility increases, but it is still not high enough to observe a change in the rate-limiting step. On the other hand, when $\nu*$ decreases with respect to ν_0, other diffusion pathways can

TABLE VI. Effective migration energies obtained from changing the attempt frequency of ω_{11}^{SO} to $\nu*$ while all other jumps have an attempt frequency equal to ν_0. When two migration energies E_m (in eV) are indicated, the first one is obtained from an Arrhenius fit of the mobility at low temperatures, while the second one is obtained from an Arrhenius fit of the mobility at high temperature. In these cases, we indicate the crossover temperature T (in K) where both Arrhenius fits intersect, indicating a change in the most probable migration mechanism.

$\nu*$		$M(V\mathrm{Xe})_T$	$M(V\mathrm{Xe})_N$	$M(V\mathrm{Kr})_T$	$M(V\mathrm{Kr})_N$
ν_0	E_m	2.99	2.98	2.88	2.87
$\frac{\nu_0}{10}$	E_m	2.99/3.14	2.99	2.88/3.03	2.88
	T	807		853	
$\frac{\nu_0}{100}$	E_m	3.01/3.22	2.99/3.24	2.89/3.14	2.88/3.13
	T	599	1054	648	973
$\frac{\nu_0}{1000}$	E_m	3.05/3.23	2.99/3.42	2.94/3.15	2.88/3.25
	T	438	841	502	734

occur (e.g., in plane trajectories). This is clearly seen in Fig. 12 where the mobility for the case $\nu* = 0.001\nu_0$ (black squares) cannot be fitted by a single Arrhenius expression. The change of slope between high- and low-temperature mobilities denotes a change of the rate-limiting step.

More insight is achieved by looking at the actual effective migration energies obtained at high and low temperature for VKr and VXe pairs, in both T and N direction, and for different values of $\nu*$. These results are shown in Table VI. As $\nu*$ decreases, the crossover temperature decreases as well, meaning that the high-temperature migration mechanisms becomes more and more probable with respect to the low-temperature one. Looking at saddle-point energies in Table III and at the diffusion network, various jumps with similar saddle-point energies could provide the high-temperature diffusion mechanism, and it is likely that they all contribute: for instance, ω_{11}^{OO}, ω_{13}^{SO}, ω_{13}^{OS}, and ω_{13}^{OO} jumps for VKr pairs (these jumps could result in effective migration energies between 3.16 and 3.29 eV); ω_{11}^{OO}, ω_{13}^{SO}, and ω_{13}^{OS} jumps for VXe pairs (these jumps could result in effective migration energies between 3.22 and 3.28 eV). These rough estimates are consistent with results from Table VI, even though not exact, because if multiple diffusion mechanisms have similar probabilities, then the kinetic correlation might significantly affect the overall diffusivity in a way that is hardly predictable beforehand. In the end, this paragraph provides orders of magnitude of attempt frequencies and temperatures where previous results might be affected.

V. CONCLUSIONS

In this study, we reported the incorporation energies of Xe and Kr in AFM UN. These solutes are found to be most stable in a Schottky defect, but due to the high formation energy of such defect, solutes are most likely to be in a uranium vacancy at equilibrium. The attraction, or repulsion, between a vacancy and these solutes was estimated by calculating the binding energy, showing a strong attraction in 1NN position, a repulsion in 2NN position, and no strong interaction for farther away configurations. Migration energies were then computed between these various configurations. The range of migration energies spreads over more than 1.5 eV for U atom jumps around a solute, but the exchange rates between a solute and a vacancy have a much higher probability than the other jump rates. For both binding and migration energy, the anisotropy created by the AFM ordering is taken into account.

These binding and migration energies were then used within the SCMF framework to obtain transport coefficients which characterize the kinetic properties of the system at the macroscopic scale. The low-migration energy for Xe and Kr exchange with a vacancy does not result in a high-diffusion coefficient because of very strong kinetic correlation effects. The energy needed for the vacancy to jump around the solute and produce long-range diffusion is the rate-limiting step. VKr and VXe pairs are strongly bound together and migrate mostly as a whole with a low probability of dissociation, which is given by flux coupling coefficients that are close to unity. Moreover, the pair migration process is efficient, more so than the migration of isolated vacancies. These highly stable and rapid vacancy-solute pairs are probably at the origin of bubble nucleation. It is also interesting to note that at the atomic scale, migration is anisotropic, whereas at a larger scale, diffusion coefficients show very little anisotropy. This is because the same atomic migration mechanism accounts for diffusion in all directions of the AFM UN.

Experimental data of solute diffusivity are not consistent, and this is most probably due to the fact that these experiments were performed on irradiated samples, where the vacancy concentration, hence solute diffusivities, is extremely sensitive to irradiation conditions. Still, our theoretical predictions seem to give lower bounds (equilibrium system) and upper bound (with vacancy concentration around 0.1 at. %) of solute diffusivity in UN. Further work on this topic is required for quantitative and meaningful comparison.

ACKNOWLEDGMENTS

The authors acknowledge support from the UIUC-KTH collaboration project INSPIRE. The authors gratefully acknowledge discussions with M. Nastar, L. Messina, D. Trinkle, and P. Bellon about the SCMF method. M. Freyss' help on the OMC scheme was very important for the completion of this paper, and we are grateful to him, E. Vathonne and M. Bertolus at CEA/DE, and B. Dorado at CEA/DAM for the implementation of this method in VASP. Funding from Svensk Kärnbränslehantering AB is acknowledged. Work by T.S. was supported by the U. S. Department of Energy (DOE), Office of Science, Basic Energy Sciences (BES) under Award No. DE-FG02-05ER46217.

APPENDIX

In this Appendix, we provide the analytical expressions of transport coefficients in a dilute tetragonally distorted fcc alloy (symmetrically equivalent to an antiferromagnetic fcc structure). It is assumed that there are no thermodynamic interactions between a vacancy and a solute beyond the 1NN configuration. For the calculation of kinetic correlations, effective interactions have also been limited to the 1NN range ($R_{\mathrm{kin}} = \sqrt{2}a$, where a is the fcc lattice parameter). This approximate model has been shown to be accurate when long-range migration is controlled by 1NN jumps only, as it is the case for Kr and Xe vacancy-mediated diffusion in UN (cf. Table V).

In the following expressions, $\zeta_{\alpha\beta\gamma}$ is a shorthand notation for the product of three (or two or one depending on the number of subscripts) jump rates: $\zeta_{\alpha\beta\gamma} = W_\alpha \times W_\beta \times W_\gamma$. W_α is the product between the probability of a configuration and the jump rate out of this configuration. Let α represent a transition state between two configurations i and j, then

$$W_\alpha = W_{ij} = p_i\omega_{ij} = p_j\omega_{ji} = \nu_\alpha \exp\left(-\frac{E_{sp}^\alpha}{k_BT}\right), \quad \text{(A1)}$$

where ω_{ij} is an atomic jump rate between configurations i and j [as in Eq. (4)], $p_i = \exp(E_b^i/k_BT)$ is the thermodynamic probability of configuration i, controlled by the binding energy of the configuration, ν_α is the attempt frequency for transition α (in s^{-1}), and E_{sp}^α is the energy at the transition state, or saddle-point energy. In the tetragonal fcc system with only 1NN interactions, there are three possible configurations with respective probabilities p_T (V and S are 1NN located in the same spin plane), p_N (V and S are 1NN perpendicular to the spin plane), and 1 (V and S do not interact). Thus, the partition function Z of the VS cluster is given by

$$Z = 4p_T + 8p_N + 7. \quad \text{(A2)}$$

The transitions are denoted by a number. Contrary to Le Claire's five-frequency model for fcc systems [65] there are eight transitions to consider here. These are sorted in two categories: in-plane jumps (jumps inside a spin plane or perpendicular to the elongation direction) and out-of-plane jumps (jumps between two spin planes or parallel to the elongation direction). The latter jumps are denoted by a hat symbol ^ above the number. Transitions 1 and $\hat{1}$ are vacancy jumps around the solute, between two 1NN configurations; transitions 2 and $\hat{2}$ correspond to vacancy-solute exchange; transitions 3 and $\hat{3}$ correspond to association (dissociation) jumps to (from) an in-plane 1NN configuration of the VS pair; transitions 4 and $\hat{4}$ correspond to association (dissociation) jumps to (from) an out-of-plane 1NN configuration of the VS pair.

Below we provide the analytical expressions for cluster transport coefficients and mobilities, both in the elongation direction (or perpendicular to spin planes, N) and in the direction perpendicular to the elongation (or inside spin planes, T). Quantities d_T and d_N are introduced to reduce the size of the expressions. Note that in order to have mobilities and transport coefficients in m^2/s the expressions below must be multiplied by the square of the lattice parameter along the diffusion direction.

Transport coefficients and mobilities of a VS pair in the N direction:

$$\begin{aligned}
d_N \times Z \times L_{VV}(VS)_N &= 2\zeta_{4\hat{2}} + 64\zeta_{\hat{4}\hat{1}} + 8\zeta_{\hat{2}\hat{3}} + 20\zeta_{\hat{4}\hat{3}} + 8\zeta_{\hat{1}\hat{3}} + 32\zeta_{\hat{4}\hat{4}} + 37\zeta_{\hat{2}\hat{4}} + 2\zeta_{\hat{2}\hat{1}} + 8\zeta_{4\hat{3}} + 20\zeta_{4\hat{4}} + 8\zeta_{4\hat{1}},\\
d_N \times Z \times L_{SS}(VS)_N &= 2\zeta_{\hat{2}4} + 5\zeta_{\hat{2}\hat{4}} + 2\zeta_{\hat{2}\hat{1}},\\
d_N \times Z \times L_{SV}(VS)_N &= -2\zeta_{\hat{2}4} - 11\zeta_{\hat{2}\hat{4}} + 2\zeta_{\hat{2}\hat{1}},\\
Z \times M(VS)_N &= \frac{\zeta_{\hat{2}\hat{1}}}{\zeta_{\hat{2}} + \zeta_{\hat{1}}},\\
d_N &= 2\zeta_4 + 2\zeta_{\hat{2}} + 5\zeta_{\hat{4}} + 2\zeta_{\hat{1}}.
\end{aligned}$$

Transport coefficients and mobility of a VS pair in the T direction:

$$\begin{aligned}
d_T \times Z \times L_{VV}(VS)_T = {} & 2\zeta_{2\hat{1}\hat{1}} + \frac{95}{2}\zeta_{23\hat{4}} + \frac{87}{2}\zeta_{3\hat{2}\hat{4}} + 16\zeta_{334} + 48\zeta_{2\hat{4}\hat{4}} + 16\zeta_{\hat{1}44} + 16\zeta_{33\hat{2}} + 40\zeta_{\hat{1}\hat{1}4} + 8\zeta_{\hat{3}\hat{3}1} + 40\zeta_{33\hat{4}} + 2\zeta_{\hat{1}\hat{1}\hat{2}}\\
& + 8\zeta_{\hat{3}\hat{3}4} + 96\zeta_{\hat{1}\hat{4}\hat{4}} + 48\zeta_{\hat{1}\hat{1}\hat{4}} + 8\zeta_{\hat{3}\hat{3}\hat{2}} + 19\zeta_{23\hat{1}} + 19\zeta_{231} + 20\zeta_{2\hat{1}\hat{3}} + 19\zeta_{234} + 4\zeta_{2\hat{1}1} + 28\zeta_{3\hat{1}\hat{3}} + 28\zeta_{2\hat{1}4}\\
& + 20\zeta_{2\hat{3}1} + 64\zeta_{3\hat{1}1} + {} + 2\zeta_{2\hat{1}\hat{2}} + 20\zeta_{2\hat{3}4} + 60\zeta_{3\hat{1}4} + 20\zeta_{2\hat{3}\hat{2}} + 40\zeta_{214} + 51\zeta_{3\hat{1}\hat{2}} + 28\zeta_{3\hat{3}4} + 80\zeta_{\hat{1}\hat{3}1}\\
& + 50\zeta_{2\hat{3}\hat{4}} + 28\zeta_{3\hat{3}\hat{2}} + 60\zeta_{314} + 64\zeta_{\hat{1}\hat{3}4} + 48\zeta_{21\hat{4}} + 26\zeta_{24\hat{2}} + 70\zeta_{3\hat{3}\hat{4}} + 80\zeta_{\hat{1}14} + 52\zeta_{24\hat{4}} + 72\zeta_{31\hat{4}}\\
& + 39\zeta_{34\hat{2}} + 152\zeta_{\hat{1}\hat{3}\hat{4}} + 4\zeta_{\hat{1}1\hat{2}} + 29\zeta_{2\hat{2}\hat{4}} + 78\zeta_{34\hat{4}} + 96\zeta_{\hat{1}1\hat{4}} + 52\zeta_{\hat{1}4\hat{2}} + 4\zeta_{\hat{3}1\hat{2}} + 104\zeta_{\hat{1}4\hat{4}} + 58\zeta_{\hat{1}\hat{2}\hat{4}}\\
& + 104\zeta_{\hat{3}4\hat{4}} + 58\zeta_{\hat{3}\hat{2}\hat{4}} + 2\zeta_{21\hat{2}} + 3\zeta_{31\hat{2}} + 96\zeta_{\hat{3}1\hat{4}} + 72\zeta_{3\hat{4}\hat{4}} + 96\zeta_{\hat{3}\hat{4}\hat{4}} + 19\zeta_{23\hat{2}} + 28\zeta_{3\hat{3}1} + 16\zeta_{331}\\
& + 80\zeta_{\hat{3}14} + 20\zeta_{\hat{3}\hat{3}\hat{4}} + 60\zeta_{\hat{1}\hat{3}\hat{2}} + 136\zeta_{3\hat{1}\hat{4}} + 40\zeta_{\hat{1}\hat{1}\hat{3}} + 52\zeta_{\hat{3}4\hat{2}} + 34\zeta_{2\hat{1}\hat{4}} + 8\zeta_{244} + 8\zeta_{\hat{1}\hat{3}\hat{3}} + 12\zeta_{344}\\
& + 16\zeta_{\hat{3}44} + 32\zeta_{3\hat{1}\hat{1}} + 16\zeta_{33\hat{1}},\\
d_T \times Z \times L_{SS}(VS)_T = {} & \frac{15}{2}\zeta_{23\hat{4}} + \frac{15}{2}\zeta_{3\hat{2}\hat{4}} + 2\zeta_{2\hat{1}\hat{1}} + 2\zeta_{\hat{1}\hat{1}\hat{2}} + 3\zeta_{23\hat{1}} + 3\zeta_{231} + 4\zeta_{2\hat{1}\hat{3}} + 3\zeta_{234} + 10\zeta_{2\hat{3}\hat{4}} + 2\zeta_{21\hat{2}} + 2\zeta_{24\hat{2}} + 3\zeta_{31\hat{2}}\\
& + 4\zeta_{\hat{1}\hat{3}\hat{2}} + 3\zeta_{34\hat{2}} + 4\zeta_{2\hat{1}4} + 4\zeta_{2\hat{3}1} + 2\zeta_{2\hat{1}\hat{2}} + 4\zeta_{2\hat{3}4} + 10\zeta_{2\hat{1}\hat{4}} + 4\zeta_{2\hat{3}\hat{2}} + 3\zeta_{3\hat{1}\hat{2}} + 4\zeta_{\hat{1}4\hat{2}} + 4\zeta_{\hat{3}1\hat{2}} + 4\zeta_{\hat{3}4\hat{2}}\\
& + 10\zeta_{\hat{1}\hat{2}\hat{4}} + 10\zeta_{\hat{3}\hat{2}\hat{4}} + 4\zeta_{2\hat{1}1} + 3\zeta_{23\hat{2}} + 4\zeta_{\hat{1}1\hat{2}} + 5\zeta_{2\hat{2}\hat{4}},\\
d_T \times Z \times L_{SV}(VS)_T = {} & -\frac{25}{2}\zeta_{23\hat{4}} - \frac{21}{2}\zeta_{3\hat{2}\hat{4}} + 2\zeta_{2\hat{1}\hat{1}} + 2\zeta_{\hat{1}\hat{1}\hat{2}} - 5\zeta_{23\hat{1}} - 5\zeta_{231} - 8\zeta_{2\hat{1}\hat{3}} - 5\zeta_{234} - 4\zeta_{2\hat{1}4} - 8\zeta_{2\hat{3}1} + 2\zeta_{2\hat{1}\hat{2}}\\
& - 8\zeta_{2\hat{3}4} - 2\zeta_{2\hat{1}\hat{4}} - 8\zeta_{2\hat{3}\hat{2}} - 20\zeta_{2\hat{3}\hat{4}} + 2\zeta_{21\hat{2}} - 6\zeta_{24\hat{2}} + 3\zeta_{31\hat{2}} - 8\zeta_{\hat{1}\hat{3}\hat{2}} - 9\zeta_{34\hat{2}} - 12\zeta_{\hat{1}4\hat{2}} + 4\zeta_{\hat{3}1\hat{2}}\\
& - 12\zeta_{\hat{3}4\hat{2}} - 14\zeta_{\hat{1}\hat{2}\hat{4}} - 14\zeta_{\hat{3}\hat{2}\hat{4}} - 5\zeta_{3\hat{1}\hat{2}} + 4\zeta_{2\hat{1}1} - 5\zeta_{23\hat{2}} + 4\zeta_{\hat{1}1\hat{2}} - 7\zeta_{2\hat{2}\hat{4}},
\end{aligned}$$

$$
\begin{aligned}
Z \times M(VS)_T &= \frac{\zeta_{2\hat{1}\hat{1}} + \zeta_{\hat{1}\hat{1}\hat{2}} + 2\zeta_{2\hat{1}1} + \zeta_{2\hat{1}\hat{2}} + \zeta_{21\hat{2}} + 2\zeta_{\hat{1}1\hat{2}}}{2\zeta_{2\hat{1}} + 2\zeta_{21} + 2\zeta_{2\hat{2}} + 4\zeta_{\hat{1}1} + 4\zeta_{\hat{1}\hat{2}} + 2\zeta_{\hat{1}\hat{1}}},\\
d_T &= 4\zeta_{2\hat{1}} + 6\zeta_{3\hat{1}} + 4\zeta_{21} + 10\zeta_{2\hat{4}} + 6\zeta_{3\hat{2}} + 8\zeta_{\hat{1}4} + 8\zeta_{\hat{3}1} + 15\zeta_{3\hat{4}} + 8\zeta_{\hat{1}\hat{2}} + 20\zeta_{\hat{1}\hat{4}} + 8\zeta_{\hat{3}\hat{2}} + 20\zeta_{\hat{3}\hat{4}} + 4\zeta_{\hat{1}\hat{1}}\\
&\quad + 8\zeta_{\hat{1}1} + 8\zeta_{\hat{3}4} + 8\zeta_{\hat{1}\hat{3}} + 4\zeta_{2\hat{2}} + 6\zeta_{34} + 4\zeta_{24} + 6\zeta_{31}.
\end{aligned}
$$

[1] K. Johnson, V. Ström, J. Wallenius, and D. Adorno Lopes (unpublished).

[2] D. L. Deforest, Transient fission gas behavior in uranium nitride fuel under proposed space applications, Technical Report, DTIC Document, 1991 (unpublished).

[3] Q. Yin, A. Kutepov, K. Haule, G. Kotliar, S. Y. Savrasov, and W. E. Pickett, Phys. Rev. B **84**, 195111 (2011).

[4] H. Wen, P.-W. Ma, and C. Woo, J. Nucl. Mater. **440**, 428 (2013).

[5] A. I. Liechtenstein, V. I. Anisimov, and J. Zaanen, Phys. Rev. B **52**, R5467 (1995).

[6] B. Meredig, A. Thompson, H. A. Hansen, C. Wolverton, and A. van de Walle, Phys. Rev. B **82**, 195128 (2010).

[7] B. Dorado, M. Freyss, B. Amadon, M. Bertolus, G. Jomard, and P. Garcia, J. Phys.: Condens. Matter **25**, 333201 (2013).

[8] H. Y. Geng, Y. Chen, Y. Kaneta, and M. Kinoshita, Phys. Rev. B **75**, 054111 (2007).

[9] D. Gryaznov, E. Heifets, and D. Sedmidubsky, Phys. Chem. Chem. Phys. **12**, 12273 (2010).

[10] G. Jomard, B. Amadon, F. Bottin, and M. Torrent, Phys. Rev. B **78**, 075125 (2008).

[11] D. Gryaznov, E. Heifets, and E. Kotomin, Phys. Chem. Chem. Phys. **14**, 4482 (2012).

[12] A. Claisse, M. Klipfel, N. Lindbom, M. Freyss, and P. Olsson, J. Nucl. Mater. **478**, 119 (2016).

[13] Z.-G. Mei, M. Stan, and B. Pichler, J. Nucl. Mater. **440**, 63 (2013).

[14] Y.-J. Zhang, J.-H. Lan, T. Bo, C.-Z. Wang, Z.-F. Chai, and W.-Q. Shi, J. Phys. Chem. C **118**, 14579 (2014).

[15] J.-H. Lan, Z.-C. Zhao, Q. Wu, Y.-L. Zhao, Z.-F. Chai, and W.-Q. Shi, J. Appl. Phys. **114**, 223516 (2013).

[16] A. Y. Kuksin, S. Starikov, D. Smirnova, and V. Tseplyaev, J. Alloys Compd. **658**, 385 (2016).

[17] M. Klipfel and P. Van Uffelen, J. Nucl. Mater. **422**, 137 (2012).

[18] Y.-J. Zhang, J.-H. Lan, C.-Z. Wang, Q.-Y. Wu, T. Bo, Z.-F. Chai, and W.-Q. Shi, J. Phys. Chem. C **119**, 5783 (2015).

[19] S. Middleburgh, P. Burr, D. King, L. Edwards, G. Lumpkin, and R. Grimes, J. Nucl. Mater. **466**, 739 (2015).

[20] A. D. Andersson, Density functional theory calculations of defect and fission gas properties in U-Si fuels, Technical Report, Los Alamos National Laboratory (LANL), 2016 (unpublished).

[21] M. J. Noordhoek, T. M. Besmann, D. Andersson, S. C. Middleburgh, and A. Chernatynskiy, J. Nucl. Mater. **479**, 216 (2016).

[22] M. J. Noordhoek, D. Andersson, and T. M. Besmann, J. Nucl. Mater. **479**, 593 (2016).

[23] É. Bévillon, R. Ducher, M. Barrachin, and R. Dubourg, J. Nucl. Mater. **434**, 240 (2013).

[24] X.-Y. Liu, B. Uberuaga, D. Andersson, C. Stanek, and K. Sickafus, Appl. Phys. Lett. **98**, 151902 (2011).

[25] M. Freyss, N. Vergnet, and T. Petit, J. Nucl. Mater. **352**, 144 (2006).

[26] A. E. Thompson and C. Wolverton, Phys. Rev. B **87**, 104105 (2013).

[27] D. Andersson, P. Garcia, X.-Y. Liu, G. Pastore, M. Tonks, P. Millett, B. Dorado, D. Gaston, D. Andrs, R. Williamson *et al.*, J. Nucl. Mater. **451**, 225 (2014).

[28] A. Schubert, K. Lassmann, P. Van Uffelen, J. Van de Laar, D. Elenkov, S. Asenov, S. Boneva, N. Djourelov, and M. Georgieva, in *Proceedings of 5th International Conference on WWER Fuel Performance, Modelling and Experimental Support, Albena, Bulgaria* (IAEA, Vienna, 2003), Vol. 29, p. 375.

[29] M. Nastar, V. Y. Dobretsov, and G. Martin, Philos. Mag. A **80**, 155 (2000).

[30] M. Nastar, Philos. Mag. **85**, 3767 (2005).

[31] T. Garnier, V. R. Manga, D. R. Trinkle, M. Nastar, and P. Bellon, Phys. Rev. B **88**, 134108 (2013).

[32] T. Garnier, M. Nastar, P. Bellon, and D. R. Trinkle, Phys. Rev. B **88**, 134201 (2013).

[33] T. Garnier, D. R. Trinkle, M. Nastar, and P. Bellon, Phys. Rev. B **89**, 144202 (2014).

[34] V. Barbe and M. Nastar, Philos. Mag. **87**, 1649 (2007).

[35] M. Nastar, Phys. Rev. B **90**, 144101 (2014).

[36] T. Schuler and M. Nastar, Phys. Rev. B **93**, 224101 (2016).

[37] M. Nastar and F. Soisson, Comprehensive Nucl. Mater. **1**, 471 (2012).

[38] A. Barbu and A. Ardell, Scr. Metall. **9**, 1233 (1975).

[39] R. Cauvin and G. Martin, J. Nucl. Mater. **83**, 67 (1979).

[40] Y. Lu, B.-T. Wang, R.-W. Li, H.-L. Shi, and P. Zhang, J. Nucl. Mater. **410**, 46 (2011).

[41] G. Kresse and D. Joubert, Phys. Rev. B **59**, 1758 (1999).

[42] J. P. Perdew, K. Burke, and M. Ernzerhof, Phys. Rev. Lett. **77**, 3865 (1996).

[43] C. Varvenne, F. Bruneval, M.-C. Marinica, and E. Clouet, Phys. Rev. B **88**, 134102 (2013).

[44] N. Curry, Proc. Phys. Soc. **86**, 1193 (1965).

[45] H. Jónsson, G. Mills, and K. W. Jacobsen, http://citeseerx.ist.psu.edu/viewdoc/summary?doi=10.1.1.31.531.

[46] A. Van der Ven, G. Ceder, M. Asta, and P. D. Tepesch, Phys. Rev. B **64**, 184307 (2001).

[47] C. S. Becquart and C. Domain, Phys. Status Solidi B **247**, 9 (2010).

[48] V. Baranov, Y. N. Devyatko, A. Tenishev, A. Khlunov, and O. Khomyakov, J. Nucl. Mater. **434**, 248 (2013).

[49] R. Oriani, Acta Metall. **18**, 147 (1970).

[50] R. B. McLellan and M. L. Wasz, Phys. Status Solidi A **110**, 421 (1988).

[51] T. Jourdan, C. C. Fu, L. Joly, J. L. Bocquet, M. J. Caturla, and F. Willaime, Phys. Scr., **T145**, 014049 (2011).

[52] J. Svoboda, Y. V. Shan, E. Kozeschnik, and F. D. Fischer, Modell. Simul. Mater. Sci. Eng. **21**, 065012 (2013).

[53] C. Barouh, T. Schuler, C.-C. Fu, and T. Jourdan, Phys. Rev. B **92**, 104102 (2015).

[54] L. Messina, M. Nastar, N. Sandberg, and P. Olsson, Phys. Rev. B **93**, 184302 (2016).

[55] M. B. Weinstein, T. A. Kirchgessner, and T. N. Tambling (unpublished).

[56] M. B. Weinstein and H. W. Davison (unpublished).

[57] J. Melehan and J. Gates, Battelle Memorial Institute, Report No. BMI-1701, 1964 (unpublished).

[58] P. Biddle, UK Atomic Energy Research Establishment, Report No. AERE-R4700, 1964 (unpublished).

[59] N. Oi, Z. Naturforsch., A **21**, 863 (1966).

[60] R. Ritzman, R. Price, R. Clark, and D. Morrison, in *Progress on Development of Fuels and Technology for Advanced Reactors*, edited by D. Keller, Atomic Energy Commission Report No. BMI-1886, 1970 (unpublished).

[61] H. Blank, Nonoxide Ceramic Nuclear Fuels, in *Materials Science and Technology* (Wiley, Weinheim, 1994).

[62] A. Booth, A method of calculating fission gas diffusion from UO_2 fuel and its application to the X-2-f loop test, Technical Report, Atomic Energy of Canada Chalk River Project, 1957 (unpublished).

[63] D. Hurst, Diffusion of Fission Gas. Calculated Diffusion from a Sphere Taking into Account Trapping and Return From the Traps, Technical Report, Atomic Energy of Canada, 1962 (unpublished).

[64] A. Lidiard, London, Edinburgh, Dublin Philos. Mag., J. Sci. **46**, 1218 (1955).

[65] A. Le Claire, J. Nucl. Mater. **69-70**, 70 (1978).

[66] D. A. Andersson, B. P. Uberuaga, P. V. Nerikar, C. Unal, and C. R. Stanek, Phys. Rev. B **84**, 054105 (2011).

[67] G. H. Vineyard, J. Phys. Chem. Solids **3**, 121 (1957).